THE JOURNAL OF PHYSICAL CHEMISTRY C

ARTICLE

pubs.acs.org/JPCC

Ga^{3+} and Y^{3+} Cationic Substitution in Mesoporous TiO_2 Photoanodes for Photovoltaic Applications

Aravind Kumar Chandiran, Frédéric Sauvage,* Lioz Etgar, and Michael Graetzel*

Laboratoire de Photonique et Interfaces, Institut des Sciences et Ingénierie Chimiques, Ecole Polytechnique Fédérale de Lausanne (EPFL), Station 6, CH-1015, Lausanne, Switzerland

Supporting Information

ABSTRACT: The optoelectronic properties of transparent nanocrystalline TiO_2 films were modified by the incorporation of a low level of Ga^{3+} or Y^{3+} cations. After optimizing their relative concentration level, we were able to increase in a noticeable manner the power conversion efficiency from 7.4% to 8.1% for gallium and even to 9.0% in the case of yttrium where all three photovoltaic (PV) performance parameters were improved simultaneously. The beneficial effect of gallium and yttrium on the PV characteristics is attributed to a lower electrical resistance and longer electron lifetime enhancing the charge collection efficiency in the transparent layer. We also herein demonstrate that the substitution of the titanium site by a trivalent element in the benchmark TiO_2 enables the disposal of the "magic" $TiCl_{4(aq)}$ post-treatment. The potential of this approach was also confirmed in solid-state PbS quantum-dot (QD) solar cells. In particular, a gallium-containing TiO_2 anatase photoanode generated twice as much short-circuit photocurrent density as the standard electrode. A 1.9% power conversion efficiency has been achieved by using a solid-state heterojunction of the doped TiO_2 with a 100 nm of PbS QD overlayer and using a gold back contact.

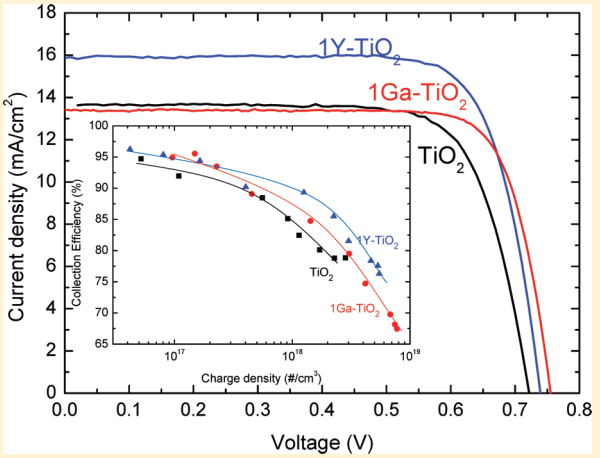

INTRODUCTION

The anatase polymorph of TiO_2 has rapidly become a leading contender in photocatalysis, electrochromic displays, and solar energy research. Its success is based not only on its appropriate band structure and optoelectronic characteristics but also arises from its ease of preparation, low cost, and environmental compatibility while being chemically robust.[1−7] The particular electronic configuration of Ti^{4+}, which adopts a $3d^0$ configuration, paves the way to a captivating multifaceted chemistry driven by its sensitiveness to crystallographic or electronic point defects. Anionic or cationic aliovalent doping of TiO_2 by means of s, p, d, or f elements has been thus intensively investigated as it allows changing to a broad extent the optoelectronic properties of the material. One goal is to push its absorption edge toward the visible domain, thus raising its photocatalytic activity in sunlight.[8−10] By contrast, this property may not be desired for regenerative solar cell applications as photocatalytic reactions could interfere with the long-term stability of the device.

Since the seminal paper reported in 1991 on mesoscopic dye-sensitized solar cell technology (DSC), the use of nanocrystals of anatase TiO_2 still prevails as material of choice for the photoanode. It is also commonly used in the related photovoltaic (PV) technologies, e.g., quantum-dot-sensitized solar cells (QDSC) or extremely thin absorber (ETA) solar cells. The mesoscopic TiO_2 film is at the heart of all these devices, playing a fundamental role for the DSC performance in light energy conversion. For instance, the roughness factor of the photoanode, given by its porosity and particle's surface area, controls the dye loading and thus the light-harvesting capability of the device. Optimization of the pore size is also highly desired to ensure efficient mass transport within the mesoporous assembly for liquid electrolyte DSC and to facilitate infiltration of the hole conductor for solid-state devices.[11,12] These different characteristics also influence the rates of electron transport vs electron recombination which control the charge collection efficiency.[13]

In order to enhance the collection of charges, several approaches have been envisaged to date, like modifying the TiO_2/electrolyte interface to reduce tri-iodide access onto the TiO_2's surface. This was carried out either by means of a coadsorbant[14−16] or by the way of a dye bearing a long aliphatic alkyl chain network.[17,18] The tailoring of more complex materials has also been particularly proficient such as a core−shell structure employing a wider bandgap shell than titania[19−23] or the reduction of the film's dimensionality to favor electron transport.[24−33] Recently, we have reported an additional route to carefully control the distribution of surface traps by the introduction of Nb^{5+} into the Ti^{4+} sites to an extent lower than 2% at.[20] This point defect entails the creation of donor states increasing the charge collection efficiency and

Received: December 21, 2010
Revised: March 4, 2011
Published: April 15, 2011

enhancing the electrode's transparency as a result of the Burstein–Moss effect.[34] We obtained higher power conversion efficiency (PCE) although the introduction of donor states decreases the output photovoltage. In this work, we pursue this approach by the inclusion of trivalent elements within the anatase lattice to create intermediate acceptor levels and evaluate whether the charge collection efficiency could be enhanced without the photovoltage penalty. Among the panel of trivalent cations on hand in the periodic table, particular attention has been paid to Ga^{3+} and Y^{3+} as these two elements were reported in the literature to not affect the optical bandgap of the anatase while presenting greater photocatalytic activity for water cleavage in comparison to the benchmark undoped TiO_2 electrode.[35−37] The photovoltaic properties of these new photoanodes will be herein presented for liquid-electrolyte-based DSCs in combination with the C101 heteroleptic ruthenium (+II) dye (Na-*cis*-Ru(4,4′-(5-hexyltiophen-2-yl)-2,2′-bipyridine)(4-carboxylic acid-4′-carboxylate-2,2′-bipyridine) (thiocyanate)$_2$)[38] as well as in solid-heterojunction PbS quantum-dot solar cells. The effect of the presence of a trivalent element on the PV characteristics will be discussed on the basis of charge extraction, photovoltage, and photocurrent transient decay measurements.

EXPERIMENTAL SECTION

a. Synthesis of TiO_2, Ga−TiO_2, and Y−TiO_2 Nanoparticles. Titanium isopropoxide (97%), gallium nitrate (99.9%), yttrium chloride (99.9%), and terpineol were obtained from Aldrich. Acetic acid, nitric acid (65%), ethyl cellulose (viscosity: 5−15, 30−50 mPas), and ethanol were purchased from Fluka. All reagents and solvents were used as received. An equimolar (0.2 mol) proportion of acetic acid (12 g) is added to titanium isopropoxide (58.6 g) under constant stirring. The trivalent precursor, corresponding to mole fraction levels with respect to titanium varying from $X = 0.5\%$ to 2% (with respect to titanium), was added dropwise under stirring. For clarity reasons, we have adopted the following terminology for the different materials synthesized: $X\%$ M^{3+}−TiO_2, where X corresponds to the amount of M^{3+} (M = Y or Ga) added into the titanium isopropoxide solution. However, as it is described in the Results and Discussion section, a discrepancy has been observed between the initial concentration of dopant in solution and its amount successfully incorporated in the anatase lattice. The intermediate product was then transferred into a conical flask containing 350 mL of water. A white precipitate was formed immediately due to hydrolysis of titanium isopropoxide and the substituent. The solution was kept under vigorous stirring for 1 h to complete the hydrolysis process. Four milliliters of concentrated HNO_3 (65%) was then added and the solution heated to 78 °C for 90 min to ensure peptization of the particles. Prior to hydrothermal reaction at 250 °C for 12 h (reactor's volume 210 mL), the solution was concentrated to 150 g using a rotovap. After the solution was cooled down to room temperature, 1 mL of concentrated HNO_3 was again added to the colloidal solution which was subsequently dispersed using a titanium ultrasonic horn for 2 min with a sequence of a 2 s long pulse and 2 s waiting time. This process is repeated three times to attain an excellent dispersion of the particles.

b. Paste Preparation. To prepare the screen printing paste, the suspension was again concentrated to 20% by weight of TiO_2; the remaining water, alcohols, and nitric acid being removed by centrifuging in ethanol. The complete procedure for screen printing paste preparation is detailed in the chart below.

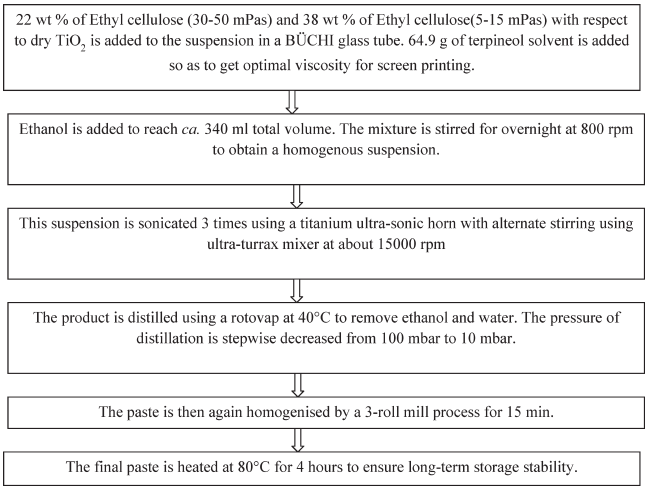

c. Synthesis of PbS Quantum Dots and Preparation of Solid-State PbS Solar Cells. Colloidal PbS nanocrystals (NCs) were purchased from Evident Technologies and stored in a nitrogen-filled glovebox. As-prepared, the PbS NCs were capped by oleic acid.

For the device fabrication, a thin blocking layer of compact TiO_2 was deposited on a cleaned fluorine-doped tin oxide (FTO) glass substrate by spray-pyrolysis using a solution of titanium diisopropoxide bis(acetylacetonate) in ethanol. The photoanode was deposited onto the compact layer by doctor blading using a diluted paste. To remove the plasticizer and terpineol, the film was sintered at 450 °C for 30 min to yield a film with thickness of 1 μm ± 100 nm. The sensitization of this layer by the quantum dots (QDs) was ensured by multilayer spin coating using 50 mg·mL^{-1} solution in octane under inert conditions. Each layer was deposited at 2500 rpm for 10 s, treated briefly with 10% 3-mercaptopropionic acid (MPA, ≥99.0% from Sigma Aldrich) in methanol (also 2500 rpm for 10 s), and rinsed with anhydrous methanol and anhydrous octane (Sigma Aldrich) to remove excess of MPA and PbS QDs. The gold contact was deposited by thermal evaporation to yield a 100 nm thick electrode.

d. Material Characterization. The structural characteristics of the different materials synthesized were analyzed by X-ray diffraction using a Bruker D8 discover diffractometer configured in a (θ−2θ) configuration with Cu $K_{\alpha 1}$ radiation (λ = 1.54056 Å). The surface area and the porosity of the films were evaluated by BET using a Micrometrics ASAP2000 apparatus with N_2 gas sorption. Prior to these measurements, the sample was degassed at 250 °C under vacuum for 4 h. The thickness of the printed film was measured using a KLA Tencor alpha-step 500 surface profiler. The optical properties were evaluated using a Cary 5 UV−visible−NIR spectrophotometer. Scanning electron microscopy (SEM) micrographs and energy dispersive X-ray (EDX) quantifications were performed using an FEI XLF30-FEG microscope. The valence state of metal ions and their atomic concentrations were probed by X-ray photoelectron spectroscopy (XPS/ESCA KRATOS AXIS ULTRA) using the Al Kα (1486.3 eV) radiation. The resistance of the TiO_2 and modified TiO_2 materials were studied using four-probes resistivity measurements. For this, condensed pellets were

shaped using a die by applying 1 ton/cm^2 pressure for 5 min using a uniaxial hydraulic press. The four-probe station is of homemade construction with probes made of Pt and (I−V) characteristics interfaced to a Keithley source meter.

The amount of dye uptake on semiconductor films was measured by dye desorption in dimethyl formamide (DMF) containing tetrabutyl ammonium hydroxide. The film area was 0.283 cm^2. The absorbance of the resulting solution was measured by UV−visible spectrophotometry (model: Hewlett−Packard 8452A diode array spectrophotometer).

e. Device Fabrication. The nanocrystalline TiO_2 films, acting as photoanode, were prepared by screen printing onto NSG10 FTO glass. Prior to screen printing, the glass was chemically treated by an aqueous solution of 40 mM of $TiCl_4$ at 70 °C for 30 min. The mesoporous films were stained with the heteroleptic ruthenium polypyridyl C101 ruthenium dye for 14 h at 4 °C in dark. The staining solution contained 300 μM of sensitizer and 75 μM of dineohexyl phosphinic acid (DINHOP) dissolved in an equimolar volume of acetonitrile and *tert*-butanol. Prior to assembling, the electrode was washed with acetonitrile. The counter electrode was made of TEC15 glass covered by ca. 50 mg/m^2 nanocrystals of PtO_x/Pt catalyst, obtained by thermal decomposition at 410 °C for 15 min of a 5 mM drop-casted solution of H_2PtCl_6 in isopropan-1-ol. The two electrodes were assembled using 25 μm thick Surlyn^{TM} polymer film. The electrolyte used was composed of 1 M 1,3 dimethylimidazole iodide (DMII), 50 mM LiI, 30 mM I_2, 0.5 M *tert*-butyl pyridine (tbp), and 0.1 M guanidinium thiocyanate (GuNCS) in a solvent mixture (85%/15% by vol.) of acetonitrile and valeronitrile. This electrolyte is injected by vacuum backfilling through a hole sand-blasted at the side of the counter electrode.

f. Photovoltaic Characterization. A 450 W xenon lamp (Oriel, U.S.) was used as a light source. The spectral output of the lamp was filtered using a Schott K113 Tempax sunlight filter (Präzisions Glas & Optik GmbH, Germany) to reduce the mismatch between the simulated and actual solar spectrum to less than 2%. The current−voltage characteristics of the cell were recorded with a Keithley model 2400 digital source meter (Keithley, U.S.). The photoactive area of 0.159 cm^2 was defined by a black metal mask. Incident photon-to-current conversion efficiency measurements were determined using a 300 W xenon light source (ILC Technology, U.S.). A Gemini-180 double monochromator Jobin Yvon Ltd. (U.K.) was used to select and increment the wavelength of the radiation illuminating the cell. The monochromatic incident light was passed through a chopper running at 1 Hz frequency, and the on/off ratio was measured by an operational amplifier. This was superimposed on a white light bias corresponding to 10 mW/cm^2 intensity. The electron recombination and transport in the mesoporous film was measured by transient photovoltage and photocurrent decay measurements, respectively. The white light was generated by an array of LEDs, while a pulsed red light (0.05 s square pulse width) was controlled by a fast solid-state switch to ascertain rapid submillisecond rise of light perturbation. The current and voltage decay was recorded on a Mac-interfaced Keithley 2602 source meter.

RESULTS AND DISCUSSION

a. Characterization of the Nanocrystalline Ga^{3+}− or Y^{3+}−TiO_2 Nanoparticles. Using the hydro(solvo)thermal procedure described in the Experimental section, white particles were recovered regardless of the nature of the substituent and its concentration. Their structural characteristics have been analyzed by powder X-ray diffraction. The collected diffractograms are gathered in Figure 1. For TiO_2, the pattern features the anatase crystal structure which crystallizes within the $I4_1/amd$ space group (tetragonal cell). The lattice cell parameters were refined using Fullprof software.[39] We obtained a value for a = 3.7856(1) Å and c = 9.5013(3) Å which is in excellent agreement with those reported in the literature.[40,41] However, a small residue between the experimental and the simulated pattern has been detected. This discrepancy was attributed to the coexistence of the rutile polymorph in a ca. 1% extent. The ratio between anatase to rutile varies noticeably depending on the nature and proportion of the substituent added along the titanium isopropoxide precursor as was observed in our previous work on niobium-doped TiO_2 photoanode.[34] Ahmad et al. have discussed this growth competition on the basis of a change in the activation energy (E_a) for the anatase-to-rutile transition when doping.[42] Based on the molar fraction of rutile polymorph (X_R) and using the proposed semiempirical relationship, $\ln X_R = -(1/T)(E_a/R)$, where T and R are the temperature and the universal gas constant, respectively. We have deduced for our benchmarch TiO_2 particles an activation energy of ca. 20.2 kJ/mol to onset this transition. In the case of gallium and yttrium, this activation energy decreases to 15.9 and 14.0 kJ/mol at a 0.5% level of Ga^{3+} and Y^{3+}, respectively. Regardless of the substituent nature and its concentration, the X-ray diffractograms (XRD) continue to feature the anatase polymorph as a major phase while the formation of Y_2O_3 or Ga_2O_3 subsequent to the hydrothermal treatment was not evidenced. The only modification noticed concerns the peak positions. This was further confirmed by their structural refinements which show a modification of the lattice cell parameter driven by the effective accommodation of the trivalent cation by the lattice (Figure 1 inset). The verification of the so-called Vegard's law attests to this successful incorporation leading to an increase of the a and c parameters in the case of the Ga^{3+} and an increase of a and a decrease along c in the case of the Y^{3+}. Nevertheless, elemental analysis performed by EDX and XPS stresses a particular discrepancy between the effective content of Ga^{3+} or Y^{3+} within the particles and their initial concentrations before the autoclaving process (initial solution was containing either 0.5, 1, or 2% of dopant concentration with respect to titanium). For instance in the case of gallium, about 60−70% of the initial amount was not incorporated in the lattice and remained unreacted in the autoclaving solution. In the solid, the rough compositions were then "$Ga_{0.13}TiO_2$", "$Ga_{0.31}TiO_2$," and "$Ga_{0.72}TiO_2$" to respectively 0.5, 1, and 2% of gallium in the pristine solution prior autoclaving (nb. charges are voluntary not compensated). For yttrium, its content in the particles is only about 0.05%, while 2% would be expected from the initial stoichiometry introduced in solution. Note that for these yttrium samples, the lattice cell parameters were constant for concentrations beyond 0.5% in solution which suggests the rapid reach of its solubility maximum. Such a low solubility limit (<0.1%) has already been evoked by Wang et al. on ceramics.[43] Although of equal charge, the difference of solubility between gallium and yttrium is ascribed to the higher ionic radii of yttrium ($r_{Y^{3+}}$ = 0.90 Å) in comparison to gallium ($r_{Ga^{3+}}$ = 0.61 Å).[44] By comparison to our precedent work on niobium where almost all this niobium was incorporated successfully ($r_{Nb^{5+}}$ = 0.64 Å),[34] the lower solubility for trivalent cations could originate from a different incorporation mechanism, notably by a different crystallographic

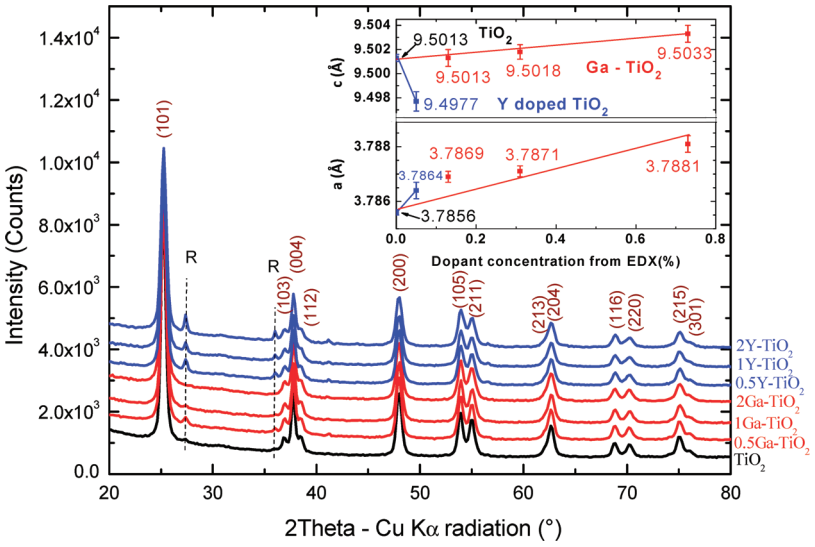

Figure 1. Superposition of the powder X-ray diffractograms for TiO_2, Ga−TiO_2, and Y−TiO_2 materials. The evolution of the lattice cell parameter refined as a function of trivalent concentration in the particles is shown in the inset.

position of the trivalent cation in the lattice or a different charge compensation mechanism (e.g., formation of O^{2-} vacancies or Ti^{4+} moving in interstitial sites). Rietveld refinement on the 2% Ga−TiO_2 sample suggests the Ga^{3+} to be positioned as a substituent of the Ti^{4+} site (4d). This looks consistent with the work of Kofstad who supported, as a generalization, that trivalent cation substitutes preferably with the Ti^{4+} site in TiO_2.[45] This is also consistent with the results published by Diamandescu et al. who were concluding the same position in the case of Fe^{3+} ($r_{Fe^{3+}}$ = 0.64 Å).[46] Unfortunately, the aforementioned low solubility of Y^{3+} has prevented us from providing any conclusive result on its crystallographic location. However, based on its significantly higher ionic radii and on its different influence on the lattice cell parameter, i.e., shrinkage along [001] direction, it seems likely that yttrium is not accommodated in a Ti^{4+} site but rather is located in an interstitial site.

XPS spectroscopy on the different samples confirms that there is no charge transfer between the substituent and the titanium. In other words, the titanium valence state remains 4+. On the other hand, for the gallium-based samples, the quantification performed by XPS suggests the formation of oxygen vacancies. Indeed, whereas the ideal stoichiometry was obtained for the pristine material $Ti^{4+}_{1.00}O^{2-}_{2.00}$, we quantified for the gallium titania sample a net stoichiometry of $Ga^{3+}_{0.01}Ti^{4+}_{0.99}O^{2-}_{1.95}$. The electroneutrality condition in this rough formula is not perfectly respected. While questions remain about the uncertainty in the quantitative measurement of the Ga−Ti to O ratio, we can also hypothesize the inappropriateness of XPS to give a statistical quantification deeper within the particles and also the formation of Schottky defects, i.e., pairs of Ti^{4+} and O^{2-} vacancies, since in the above formula was assumed all the cationic site to be occupied. Nevertheless, the results for gallium clearly suggest the formation of oxygen vacancies, their concentration [$V_{\ddot{O}}$] being fixed by the concentration of Ga^{3+} in the crystal as similarly described in the literature in the case of the rutile polymorph.[47] The generation of an oxygen-deficient material is consistent with the decrease in the activation energy for the anatase-to-rutile transition[48] and is also in agreement with the thermopower measurements performed on all the samples showing a n-type behavior. In the absence of strong evidence for Schottky defects in the material, at the present stage, the incorporation mechanism for the gallium can be written using the Kröger−Vink notation as being

$$Ga^{3+}_{solvated} + Ti^{x}_{Ti}(TiO_2) \rightarrow \left[Ga'_{Ti} + \frac{1}{2}V_{\ddot{O}}\right](TiO_2)$$

The incorporation of Ga^{3+} and Y^{3+} entails a small decrease of crystallite size as similarly experienced in the case of niobium doping.[34] Table 1 summarizes all the particle characteristics, including the BET surface area based on N_2 desorption, crystallite size calculated from the [200] and [004] directions, and particle size and film porosity measured on the screen-printed film. The latter lies between 69 and 72% with the exception of the 1% and 2% Y−TiO_2 samples for which the electrode's porosity decreased to 65% and 64%, respectively. The BET surface area of the different samples is between 78 and 85 m^2/g.

Figure 2 compares at the same magnification the SEM micrograph for TiO_2, 2% Ga−TiO_2, and 2% Y−TiO_2 mesoporous film. Regardless of the substituent, the film is composed of nanoparticles of around 20 nm size, leaving mesopores ranging from 20 to 30 nm diameter particularly suitable to guarantee high dye loading and efficient mass transport all through the pores. For a concentration of $YCl_3 \cdot 3H_2O$ greater than 1%, we have observed the remains of small aggregated particles (see Figure 2c). This could be at the origin of the decrease in the electrode's porosity. By taking into account the contribution of anisotropic and strain broadening in the profile of the XRD peaks in our Rietveld refinement, the average morphology of the particles was modeled using a G-Fourier program. The results for TiO_2 and 2% Ga−TiO_2 are shown in the inset of Figure 2. The incorporation of gallium entails a slight modification of the particle's morphology which depicts a bulged elliptical shape. From an optical point of view, a bandgap of 3.22 eV has been measured for our TiO_2 which is in excellent agreement with the values reported in the literature[49] (see Figure 1 in the Supporting Information). This value is not modified noticeably by the substitution with Ga^{3+} (3.19−3.25 eV). Interestingly, this contrasts with the case of yttrium-doped anatase, where the bandgap

dx.doi.org/10.1021/jp1121068 |J. Phys. Chem. C 2011, 115, 9232–9240

Table 1. Evolution of Crystallite Size, BET Surface Area, Particle Size, and Film Porosity for TiO_2, Ga−TiO_2, and Y−TiO_2 Samples[a]

	crystallite size (nm)				
sample	[004]	[200]	BET surface area (m^2/g)	particle size (nm)	film porosity (%)
TiO_2	15.4	25.0	78	20.1	69
0.5% Ga−TiO_2	15.3	25.9	78	20.0	69
1% Ga−TiO_2	14.9	23.2	79	19.8	72
2% Ga−TiO_2	13.2	22.3	85	18.3	71
0.5% Y−TiO_2	14.0	22.4	83	18.8	70
1% Y−TiO_2	14.0	21.9	84	18.5	65
2% Y−TiO_2	13.9	22.0	85	18.4	64

[a] nb. Characteristics given without any $TiCl_4$ post-treatment.

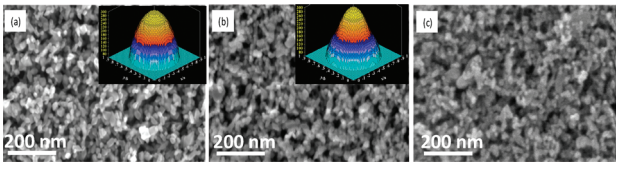

Figure 2. SEM micrograph for (a) TiO_2 (b) 2% Ga−TiO_2, and (c) 2% Y−TiO_2 films. In the inset is shown the particle shape reconstruction from Rietveld analysis.

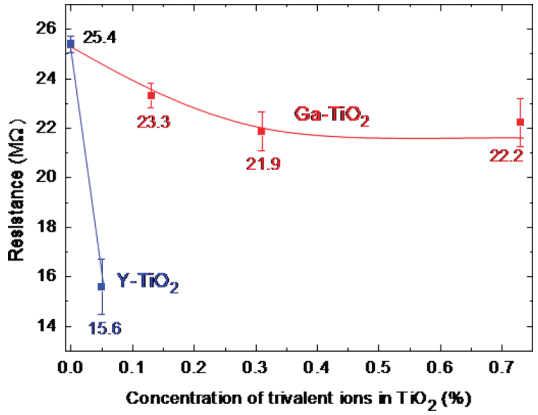

Figure 3. Evolution of the direct current (dc) resistance for TiO_2, Ga−TiO_2, and Y−TiO_2 pressed pellet.

decreases to 3.12 eV and even to 2.97 eV for the 0.5−1% Y−TiO_2 and 2% Y−TiO_2, respectively. Such a difference may hint of a different position held by yttrium in the lattice. The point defect created by the introduction of gallium or yttrium leads to a slight increase in the film's conductivity. Figure 3 shows the evolution of the resistance measured on a compact pellet using a Pt four-probe technique. For TiO_2, the resistance measured corresponds to a mean value of 25.4 ± 0.3 MΩ. The incorporation of gallium decreases this value by around 3 MΩ whereas the effect of yttrium on the conductivity was more pronounced with a final value reaching 15.6 ± 1.1 MΩ. This decrease of resistivity is relatively surprising since theoretically we would expect the formation of oxygen vacancies to strengthen the trapping effect of the electron nearby the transition metal orbitals. Further experiments to study the transport properties in these new nanocrystals are underway to better understand the mechanism by which the charges are transported.

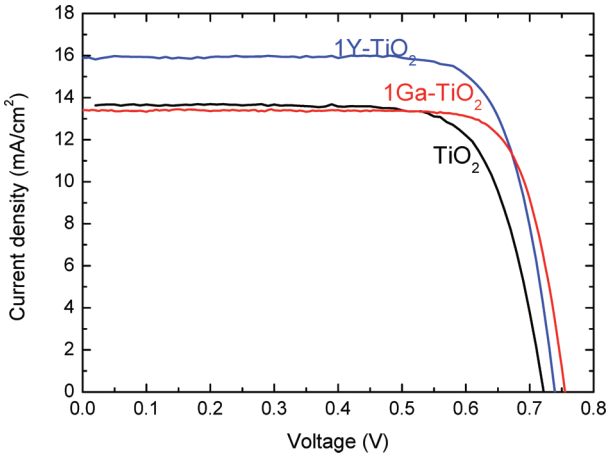

Figure 4. ($J-V$) curve measured under 100 mW/cm^2 illumination (Air Mass 1.5 G conditions) for 7 μm thick transparent electrode of TiO_2, 1% Ga−TiO_2, and 1% Y−TiO_2 sensitized with C101 dye.

Table 2. PV Characteristics for the Standard TiO_2 and Ga−TiO_2 Films without $TiCl_4$ Post-Treatment

sample	TiO_2	0.5% Ga−TiO_2	1% Ga−TiO_2	2% Ga−TiO_2
V_{OC} (mV)	721	732	755	768
J_{SC} (mA/cm^2)	13.6	12.7	13.4	11.3
ff (%)	75	76	79	80
η (%)	7.4	7.2	8.1	7.0

b. Photovoltaic Properties in Liquid C101-Sensitized Solar Cells. The new photoanodes were incorporated in dye-sensitized solar cells in combination with the recently developed C101 Ru(+II) dye and tested with a volatile liquid electrolyte. The particularity of this dye, related to the family of Z907Na, lies in its higher molar extinction (17 500 $M^{-1}\cdot cm^{-1}$) and red-shifted metal-to-ligand charge transfer (MLCT) transition at 547 nm.[38] The improvement of the dye's optical properties results from the destabilization of the metal-t_{2g} orbitals by the electron-rich thiophene group attached to the bipyridine ancillary ligand. Throughout this work, the photoanode consisted of a 7 μm thick transparent nanocrystalline TiO_2 film. No light scattering layer was superimposed in order to probe clearly the effect of modifying the anatase with the trivalent substituents. Under these conditions, the standard TiO_2 photoanode without $TiCl_4$ post-treatment exhibits a power conversion efficiency at full AM 1.5G sunlight of 7.4% (J_{SC} = 13.6 mA/cm^2, V_{OC} = 721.4 mV, and ff = 74.6%) (Figure 4 and Table 2). Substitution of Ti^{4+} by Ga^{3+} improves the V_{OC} from 721.4 to 768.3 mV and the fill factor from 74.6% to 80.4%. Although an increase of the photovoltage often entails a decrease of short-circuit current density due to insufficient driving force for electron injection, in this case the photocurrent was maintained at 13.4 mA/cm^2 up to a doping level of 1% Ga−TiO_2 before it dropped to 11.3 mA/cm^2. Optimal performance was reached by the 1% Ga−TiO_2 material, achieving a substantial PCE improvement from 7.4% to 8.1%.

The effect of yttrium is again different in as much as its presence enhances both the short-circuit photocurrent and the fill factor (Table 3). A maximum of J_{sc} = 15.9 mA/cm^2 was

obtained for the 1% Y−TiO_2 sample. In contrast to the effect of gallium, the photovoltage is relatively constant, increasing only slightly for the 1% Y−TiO_2 material to 739 mV before it declines to 708 mV at higher yttrium levels. By improving the three key PV parameters simultaneously, the use of the 1% Y−TiO_2 particles enables a PCE as high as 9.0%.

In order to attain their optimal performance, nanocrystalline anatase films are normally subjected to a post-treatment by a solution of $TiCl_{4(aq)}$ which produces a layer of TiO_2 nanocrystals of 2−3 nm in size at the surface of the anatase particles increasing the electrode's roughness factor and therefore the dye loading. In addition this post-treatment augments the necking between the TiO_2 nanoparticles reducing the rate of the back-reaction.[34,50,51] These beneficial effects were also verified in this work since the $TiCl_{4(aq)}$ post-treatment improved the PCE remarkably from 7.4 to 8.4% owing to a gain of photovoltage and photocurrent (Table 4).

For the new photoanodes developed in this work, this post-treatment still benefits the photocurrent. However, it decreases both the fill factor value and the photovoltage. As the gain in J_{sc} compensates the loss of V_{OC} and ff, the final PCE shows only a slight increase to 9.1%. It remains to be explored why the $TiCl_{4(aq)}$ post-treatment affects differently the doped anatase layers compared to the benchmark samples. These findings have great practical importance as they render superfluous the additional post-treatment of the particles simplifying the cell manufacturing while affording improved power conversion efficiency.

The incident photon-to-electric current conversion efficiency (IPCE) was measured for TiO_2, 1% Ga−TiO_2, and 1% Y−TiO_2 between 340 and 750 nm (Figure 5). For the TiO_2 reference, the IPCE spectrum shows a broad feature ranging from 380 to 750 nm characteristic of the C101 dye. The maximum IPCE is 82% at 550 nm. Devices assembled with the Ga-doped TiO_2 show a very similar feature, a slightly lower yield in the blue part of the spectrum being compensated to some degree by an increase in the red. On the other hand, major improvements are noticed with the 1% Y−TiO_2 material, which exhibits an enhanced red response and a maximum of conversion reaching 90% at 550 nm. These results are consistent with the trends of the short-circuit current density recorded with our solar simulator.

In order to gain more insight into the origin of the observations for the PV characteristics made with the new photoanodes, we have first carefully measured the amount of dye chemisorbed onto the mesoporous film. For this, we probed the visible light absorption given by the MLCT transition of the dye desorbed in a DMF solution of *tert*-butyl ammonium hydroxide. The values obtained are tabulated in Table 5. The electrode composed of our regular TiO_2 accommodated 6.8×10^{-8} mol/cm^2 of C101 molecules compared to 6.2×10^{-8} mol/cm^2 for 0.5% Ga−TiO_2. The dye loading increases along the level of Ga-substituent to reach 7.3×10^{-8} mol/cm^2 for 2% Ga−TiO_2. The trend in the short-circuit current density matches the dye loading, except for the sample containing 2% Ga−TiO_2. Since the Ga-doped films have comparable BET surface area and porosity, the effect of gallium on the dye loading appears to result from a change in the acid−base behavior of the material, possibly an increase in the isoelectric point favoring dye uptake.

For yttrium, the higher dye loading could result in part from the larger roughness factor of the electrode. However, the marked augmentation of the short-circuit current density cannot be rationalized by an increase of the film's optical density alone. This is the reason why we pursued our investigation using the

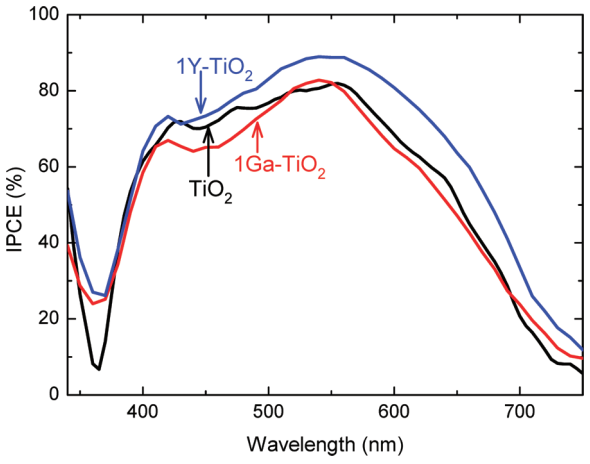

Figure 5. IPCE spectra recorded on 7 μm thick transparent electrode of TiO_2, 1% Ga−TiO_2, and 1% Y−TiO_2 sensitized with C101 dye.

Table 3. PV Characteristics for the Standard TiO_2 and Y−TiO_2 Films without $TiCl_4$ Post-treatment

sample	TiO_2	0.5% Y−TiO_2	1% Y−TiO_2	2% Y−TiO_2
V_{OC} (mV)	721	718	739	708
J_{SC} (mA/cm^2)	13.6	14.4	15.9	14.7
ff (%)	75	78	77	75
η (%)	7.4	8.0	9.0	7.9

Table 5. Dye Loading upon 7 μm Thick Films of TiO_2 and Substituted TiO_2[a]

	dye concentration ($\times 10^{-8}$ mol/cm^2)	
sample	M = Ga^{3+}	M = Y^{3+}
TiO_2	6.8	6.8
0.5% M−TiO_2	6.2	7.5
1% M−TiO_2	6.9	8.0
2% M−TiO_2	7.3	7.6

[a] Values given without $TiCl_4$ post-treatment.

Table 4. Comparison of the PV Characteristics for TiO_2, 1% Ga−TiO_2, and 1% Y−TiO_2 before and after $TiCl_4$ Post-treatment

	TiO_2		1% Ga−TiO_2		1% Y−TiO_2	
sample	no $TiCl_4$ treatment	$TiCl_4$ post-treatment	no $TiCl_4$ treatment	$TiCl_4$ post-treatment	no $TiCl_4$ treatment	$TiCl_4$ post-treatment
V_{OC} (mV)	721	740	755	743	739	733
J_{SC} (mA/cm^2)	13.6	15.3	13.4	14.0	15.9	16.9
ff (%)	75	73	79	78	77	74
η (%)	7.4	8.4	8.1	8.1	9.0	9.1

dx.doi.org/10.1021/jp1121068 |*J. Phys. Chem. C* 2011, 115, 9232–9240

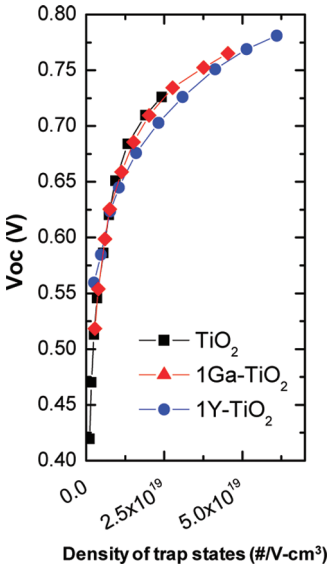

Figure 6. Distribution of density of electron trapping states in TiO_2, 1% Ga−TiO_2, and 1% Y−TiO_2 films sensitized by the C101 dye.

charge extraction measurements to assess the distribution and density of surface states within the new materials. Conversely to the case of niobium which creates intraband donor states,[34] the substitution of titanium by gallium or yttrium does not influence the density and energy distribution of the trap states below the conduction band (Figure 6). Deduced from the single exponential photovoltage decay, Figure 7a shows the evolution of the electron lifetime as a function of the charge density within the film. These results underline the effectiveness of the trivalent cations to increase the electron lifetime several times, most notably at high charge densities. For instance, at a charge density of 10^{18} #/cm^3, the electron lifetime measured in the standard TiO_2 film is 18 ms compared to 55 ms for the Y^{3+} and Ga^{3+} samples, the latter being most efficient in retarding the electron back-reaction. Altogether, these results suggest that the observed increase of photovoltage can be assigned to the longer electron lifetime and not to an upward shift of the conduction band edge.

The photocurrent decay at short-circuit condition was also measured to analyze the dynamics of the electron transport process. The evolution of transport rate (k_t) as a function of charge density is plotted in Figure 7b. Clearly the trivalent cations retard the charge transport. Thus, for a charge density of 10^{18} #/cm^3, the rate constant for our standard TiO_2 is ca. 379 s^{-1} whereas it decreases to 171 s^{-1} for yttrium and 111 s^{-1} for gallium. The charge collection efficiency (η_{CE}) is given by the ratio of the transport rate and the sum of transport and recombination rate. Results are reported in Figure 7c as a function of charge density. For a charge density of 10^{18} #/cm^{-3}, the collection efficiency in our nanocrystalline TiO_2 attains 84% in comparison to 87% and 90% for 1% Ga−TiO_2 and 1% Y−TiO_2, respectively. The latter material gives the best compromise between prolonging the electron lifetime and maintaining fast electron transport. Clearly, introducing these trivalent cations is beneficial to enhance the charge collection efficiency and therefore the PCE.

c. Photovoltaic Properties in Solid-State PbS Quantum-Dot Solar Cells. Based on these encouraging results, the best performing gallium- and yttrium-modified TiO_2 materials have also been introduced as electron collectors in solid-state quantum-dot heterojunction solar cells. Among the different colloidal

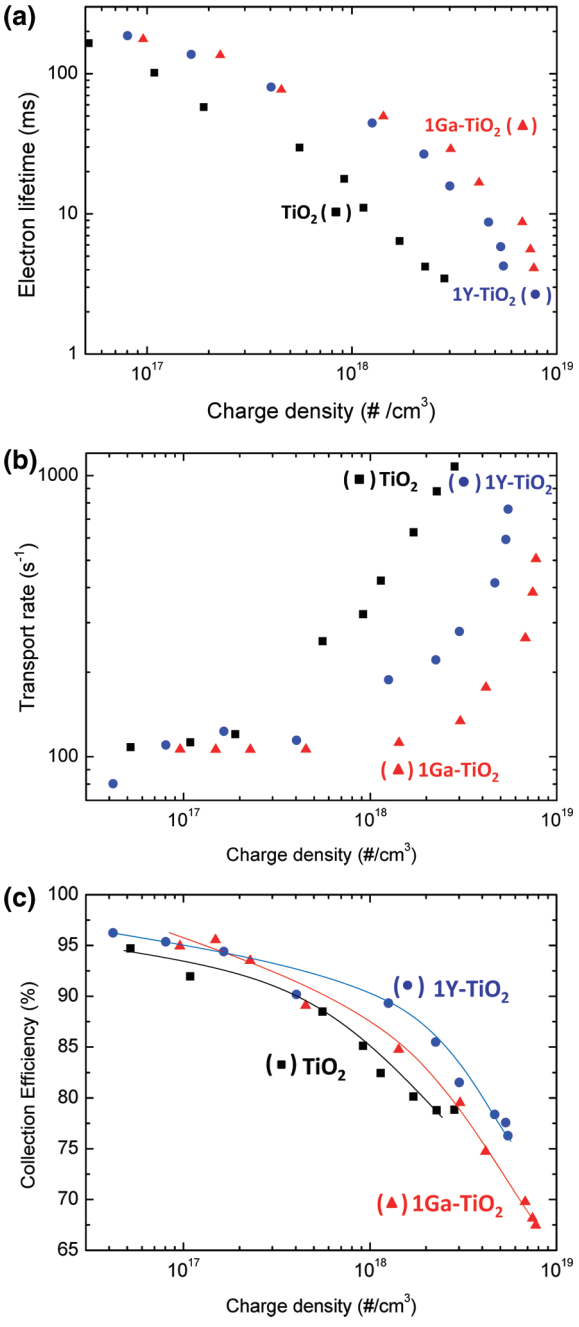

Figure 7. Evolution of (a) electron lifetime, (b) transport rate, and (c) charge collection efficiency as a function of electron charge density for the standard TiO_2, 1% Ga−TiO_2, and 1% Y−TiO_2 films.

semiconductor nanocrystals that have been developed to date, we turned toward lead chalcogenides nanocrystals as this family exhibits high dielectric constant and therefore large exciton Bohr radius which paves the way to a significant degree of quantum confinement affording bandgap values from 0.5 to 2 eV.[52−56] The other advantage of PbX over the other QDs lies in the small effective masses for the electrons and holes (i.e., < 0.09 me). This characteristic is particularly beneficial to ensure an efficient charge delocalization in the QD film with high carrier mobility. In contrast to the solid-state dye-sensitized solar cells where the liquid electrolyte is replaced by the Spiro-OMeTAD as a hole conductor and basically set in association with a high molar

dx.doi.org/10.1021/jp1121068 |J. Phys. Chem. C 2011, 115, 9232–9240

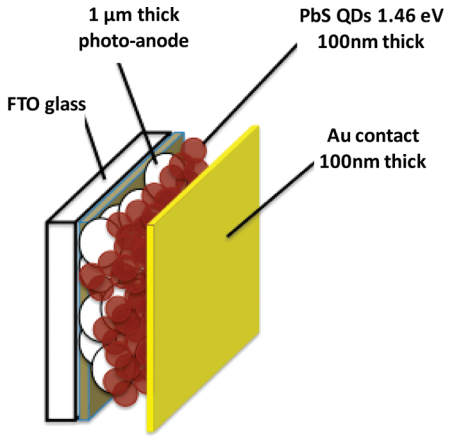

Figure 8. Schematic representation of the TiO_2/PbS/Au solid-state heterojunction solar cells.

Table 6. Comparison of the Photovoltaic Characteristics Using TiO_2, 1% Ga−TiO_2, and 1% Y−TiO_2 Photoanode in PbS/Au Solid-State Quantum-Dot Solar Cells

sample	TiO_2	1% Y−TiO_2	1% Ga−TiO_2
V_{OC} (mV)	507	502	485
J_{SC} (mA/cm^2)	5.2	6.5	11.1
ff (%)	25	32	35
η (%)	0.7	1.0	1.9

extinction coefficient organic sensitizer, PbS quantum dots, used in this survey, operate as both a light absorber and a hole conductor (Figure 8). The photovoltaic properties have been examined using standard 20 nm-based TiO_2 particles and compared to the 1% Ga−TiO_2 or 1% Y−TiO_2 nanoparticles. A ca. 200 nm thick layer of PbS quantum dots was spin-coated onto the surface of the mesoscopic titania film. A thin gold layer was evaporated onto the PbS nanocrystals under vacuum. To the best of our knowledge, this is the first time that modified TiO_2 film of this type has been employed as such a heterojunction QD solar cell. Table 6 gathers all the photovoltaic characteristics of the photoanodes used. The PV properties of both the gallium− and yttrium−TiO_2 electrodes outperform that of TiO_2. The most striking result comes from the 1% Ga−TiO_2 where the short-circuit current density was significantly improved from 5.2 to 11.1 mA/cm^2, albeit at the expense of the photovoltage which decreased from 507 to 485 mV (Figure 9). Note that the fill factor was also substantially increased from 0.25 to 0.35. These characteristics bring the PCE to 1.9% in comparison to 0.7% for the benchmark TiO_2 alone. In contrast to the liquid electrolyte, the gallium-based sample shows the best results here. The incorporation of the yttrium-based TiO_2 nanoparticles was also beneficial to increase the short-circuit current density (J_{sc} = 6.5 mA/cm^2) and the fill factor (ff = 0.32) leading to a PCE of 1.0%. We speculate that the prolongation of the electron lifetime in these new photoanodes augments substantially the charge carrier collection efficiency and hence the short-circuit current density. Further experiments are underway to scrutinize the role of trivalent cation in enhancing the performance of TiO_2/PbS heterojunction solar cells.

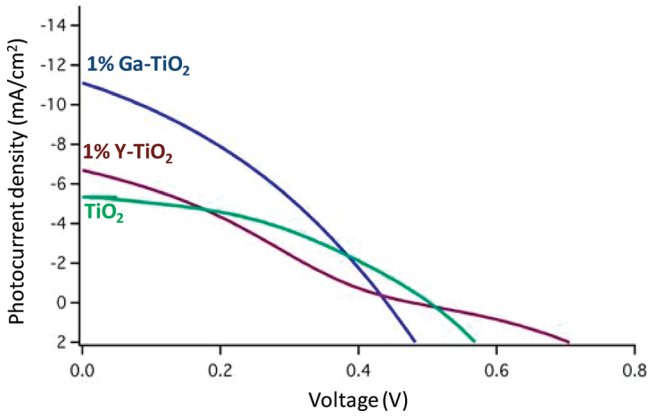

Figure 9. ($J-V$) curve measured under 100 mW/cm^2 illumination (Air Mass 1.5 G conditions) for TiO_2/PbS/Au, 1% Ga−TiO_2/PbS/Au, and 1% Y−TiO_2/PbS/Au heterojunction solar cells.

CONCLUSION

We modified the optoelectronic properties of regular anatase TiO_2 nanocrystals by means of aliovalent doping by Ga^{3+} or Y^{3+}. Their successful incorporation within the anatase lattice was confirmed notably by powder X-ray diffraction with the verification of the Vegard's law. Rietveld refinement carried out in the case of the Ga^{3+} sample suggests the latter to substitute Ti^{4+} lattice ions entailing the formation of oxygen vacancies. In the case of yttrium, the location in the host lattice remains unclear to date owing to its very restricted solubility (ca. 0.05%). In conjunction with the C101 dye in liquid-electrolyte-based dye-sensitized solar cells, higher power conversion efficiencies were obtained with these new photoanodes, the champion cell being the 1% Y−TiO_2 sample showing 9.1% PCE. The improvement in performance was ascribed to an increase of electron lifetime in the new photoanodes which affords close to unity charge collection efficiency. The addition of these dopants renders superfluous the post-treating of the particles with a $TiCl_{4(aq.)}$. Finally, we have also performed preliminary tests employing the modified TiO_2 particles as electron collector in solid-state TiO_2/PbS QDs heterojunction solar cells. The best result was so far achieved with a gallium-based photoanode leading to 1.9% PCE in comparison to 0.7% obtained using regular TiO_2 nanoparticles.

ASSOCIATED CONTENT

Supporting Information. UV−vis absorption spectrum of TiO_2 and the different gallium- and yttrium-based TiO_2 photoanodes. This material is available free of charge via the Internet at http://pubs.acs.org.

AUTHOR INFORMATION

Corresponding Author

*E-mail: frederic.sauvage@u-picardie.fr (F.S.); michael.graetzel@epfl.ch (M.G.).

ACKNOWLEDGMENT

A.K.C., F.S., and M.G. thank Dr. S. M. Zakeeruddin and Pr. Peng Wang for providing us with C101 dye solution and electrolyte and Pascal Comte and Dr. R. Humphry-Baker for

fruitful discussions. We also thank Dr. Montserrat Casas-Cabanas for her contribution with the Rietveld refinement and Dr. Md. K. Nazeeruddin. The authors also acknowledge financial support of this work by EU project "ROBUST DSC" grant agreement number 212792 and "INNOVASOL" with grant agreement number 227057. A.K.C. is indebted to EACEA, Brussels for the financial support of the Erasmus-Mundus Master Course M. ESC program (Materials for Energy Storage and Conversion). L. E. acknowledges the Marie Curie actions-intra European fellowships (FP7-PEOPLE-2009IEF) under the grant agreement number 25220 "Excitonic Solar Cells".

REFERENCES

(1) Fujishima, A.; Honda, K. *Nature* **1972**, *238*, 37.
(2) Borgarello, E.; Kiwi, J.; Pelizzetti, E.; Visca, M.; Graetzel, M. *Nature* **1981**, *289*, 158.
(3) Khan, S. U. M.; Akikusa, J. *J. Phys. Chem. B.* **1999**, *103*, 7184.
(4) Khaselev, O.; Turner, J. A. *Science* **1998**, *280*, 425.
(5) Asahi, R.; Morikawa, T.; Ohawaki, T.; Aoki, K.; Taga, Y. *Science* **2001**, *293*, 269.
(6) Palmisano, G.; Augugliaro, V.; Pagliaro, M.; Palmisano, L. *Chem. Commun.* **2007**, 3425.
(7) O'Regan, B.; Graetzel, M. *Nature* **1991**, *353*, 737.
(8) Ghosh, A. K.; Maruska, H. P. *J. Electrochem. Soc.* **1997**, *124* (10), 1516.
(9) Maruska, H. P.; Ghosh, A. K. *Sol. Energy Mater.* **1979**, *1*, 237–247.
(10) Stalder, C.; Augustynski, J. *J. Electrochem. Soc.* **1979**, *126* (11), 2007.
(11) Zakeeruddin, S. M.; Graetzel, M. *Adv. Funct. Mater.* **2009**, *19*, 2187–2202.
(12) Ding, I. K.; Tétreault, N.; Brillet, J.; Hardin, B. E.; Smith, E. H.; Rosenthal, S. J.; Sauvage, F.; Graetzel, M.; McGehee, M. D. *Adv. Funct. Mater.* **2009**, *19*, 2431–2436.
(13) Peter, L. M. *Phys. Chem. Chem. Phys.* **2007**, *9*, 2630.
(14) Wang, M.; Graetzel, C.; Moon, S. J.; Humphry-Baker, R.; Rossier-Iten, N.; Zakeeruddin, S. M.; Graetzel, M. *Adv. Funct. Mater.* **2009**, *19*, 2163.
(15) Wang, P.; Zakeeruddin, S. M.; Humphry-Baker, R.; Moser, J. E.; Graetzel, M. *Adv. Mater.* **2003**, *15* (24), 2101.
(16) Yum, J. H.; Jang, S.; Humphry-Baker, R.; Graetzel, M.; Cid, J. J.; Torres, T.; Nazeeruddin, M. K. *Langmuir* **2008**, *24*, 5636.
(17) Zakeeruddin, S. M.; Nazeeruddin, M. K.; Humphry-Baker, R.; Pechy, P.; Quagliotto, C.; Barolo, C.; Viscardi, G.; Graetzel, M. *Langmuir* **2002**, *18*, 952.
(18) Nazeeruddin, M. K.; Zakeeruddin, S. M.; Lagref, J. J.; Liska, P.; Comte, P.; Barolo, C.; Viscardi, G.; Schenk, K.; Graetzel, M. *Coord. Chem. Rev.* **2004**, *248* (13−14), 1317–1328.
(19) Devries, M. J.; Pellin, M. J.; Hupp, J. T. *Langmuir* **2011**, *26*, 9082–9087.
(20) Palomares, E.; Clifford, J. N.; Haque, S. A.; Lutz, T.; Durrant, J. R. *Chem. Commun.* **2002**, *14*, 1464.
(21) Greff, B. A.; Pichot, F.; Ferrere, S.; Fields, C. L. *J. Phys. Chem. B.* **2001**, *105*, 1422.
(22) Li, T. C.; Goes, M. S.; Fabregat-Santiago, F.; Bisquert, J.; Bueno, P. R.; Prasittichai, C.; Hupp, J. T.; Marks, T. J. *J. Phys. Chem. C* **2009**, *113* (42), 18385.
(23) Kay, A.; Graetzel, M. *Chem. Mater.* **2002**, *14* (7), 2930.
(24) Zhu, K.; Neale, N. R.; Miedaner, A.; Frank, A. J. *Nano Lett.* **2007**, *7*, 69–74.
(25) Prakasam, H. E.; Shankar, K.; Paulose, M.; Varghese, O. K.; Grimes, C. A. *J. Phys. Chem. C* **2007**, *111*, 7235–7241.
(26) Jennings, J. R.; Ghicov, A.; Peter, L. M.; Schmuki, P.; Walker, A. B. *J. Am. Chem. Soc.* **2008**, *130*, 13364–13372.
(27) Kim, D.; Ghicov, A.; Albu, S. P.; Schmuki, P. *J. Am. Chem. Soc.* **2008**, *130*, 16454–16455.
(28) Mor, G. K.; Kim, S.; Paulose, M.; Varghese, O. K.; Shankar, K.; Basham, J.; Grimes, C. A. *Nano Lett.* **2011**in press.
(29) Feng, X.; Shankar, K.; Varghese, O. K.; Paulose, M.; Latempa, T. J.; Grimes, C. A. *Nano Lett.* **2008**, *8*, 3781–3786.
(30) Varghese, O. K.; Paulose, M.; Grimes, C. A. *Nat. Nanotechnol.* **2009**, *4*, 592.
(31) Zhang, Q. F.; Dandeneau, C. S.; Zhou, X. Y.; Cao, G. Z. *Adv. Mater.* **2009**, *21*, 4087–4108.
(32) Qian, J.; Liu, P.; Xiao, Y.; Jiang, Y.; Cao, Y.; Ai, X.; Yang, H. *Adv. Mater.* **2009**, *21*, 3663–3667.
(33) Sauvage, F.; Di Fonzo, F.; Li Bassi, A.; Casari, C. S.; Russo, V.; Divititi, G.; Ducati, C.; Bottani, C. E.; Comte, P.; Graetzel, M. *Nano Lett.* **2010**, *10* (7), 2562–2567.
(34) Chandiran, A. K.; Sauvage, F.; Casas-Cabanas, M.; Comte, P.; Zakeeruddin, S. M.; Graetzel, M. *J. Phys. Chem. C* **2010**, *114*, 15849.
(35) Li, J.; Yang, X.; Yu, X.; Xu, L.; Kang, W.; Yan, W.; Gao, H.; Liu, Z.; Guo, Y. *Appl. Surf. Sci.* **2009**, *255*, 3731–3738.
(36) Houlihan, J. F.; Armitage, D. B.; Hoovler, T.; Bonaquist, D. *Mater. Res. Bull.* **1978**, *13*, 1205–1212.
(37) Augustynski, J.; Hinden, J.; Stalder, C. *J. Electrochem. Soc.* **1977**, *124* (7), 1063–1064.
(38) Gao, F.; Wang, Y.; Shi, D.; Zhang, J.; Wang, M.; Jing, X.; Humphry-Baker, R.; Wang, P.; Zakeeruddin, S. M.; Graetzel, M. *J. Am. Chem. Soc.* **2008**, *130*, 10720.
(39) Roisnel, T.; Rodriguez-Carjaval, J. *Fullprof* (v. 2008), France.
(40) Burdett, J. K.; Hughbanks, T.; Miller, G. J.; Richardson, J. W.; Smith, J. V. *J. Am. Chem. Soc.* **1987**, *109* (12), 3639.
(41) Howard, C. J.; Sabine, T. M.; Dickson, F. *Acta Crystallogr.* **1991**, *B47*, 462.
(42) Ahmad, A.; Buzby, S.; Ni, C.; Ismat Shah, S. *J. Nanosci. Nanotechnol.* **2008**, *8* (5), 2410.
(43) Wang, Q.; Lian, G.; Dickley, E. C. *Acta Mater.* **2004**, *52*, 809–820.
(44) Shannon, R. D. *Acta Crystallogr.* **1976**, *A32*, 751.
(45) Kofstad, P. *J. Less-Common Met.* **1967**, *13*, 635.
(46) Diamandescu, L.; Vasiliu, F.; Tarabasanu-Mihaila, D.; Feder, M.; Vlaicu, A. M.; Teodorescu, C. M.; Macovei, D.; Enculescu, I.; Parvulescu, V.; Vasile, E. *Mater. Chem. Phys.* **2008**, *112*, 146–153.
(47) Okajima, T.; Yamamoto, T.; Kunisu, M.; Yoshioka, S.; Tanaka, I.; Umesaki, N. *Jpn. J. Appl. Phys.* **2006**, *45* (9), 7028–7031.
(48) Malati, M. A.; Wong, W. K. *Surf. Technol.* **1984**, *22*, 305–322.
(49) Sanjinés, R.; Tang, H.; Berger, H.; Gozzo, F.; Margaritondo, G.; Levy, F. *J. Appl. Phys.* **1994**, *75* (6), 2945.
(50) Zhu, K.; Kopidakis, N.; Neale, N. R.; Lagemaat, J. V.; Frank, A. J. *J. Phys. Chem. B.* **2006**, *110* (50), 25174.
(51) O'Regan, B.; Durrant, J. R.; Sommeling, P. M.; Bakker, N. J. *J. Phys. Chem. C.* **2007**, *111*, 14001.
(52) Wise, F. W. *Acc. Chem. Res.* **2000**, *33*, 773.
(53) Hines, M. A.; Scholes, G. D. *Adv. Mater.* **2003**, *15*, 1844.
(54) Evans, C. M.; Guo, L.; Peterson, J. J.; Maccagnano-Zacher, S.; Krauss, T. D. *Nano Lett.* **2008**, *8*, 2896.
(55) Pietryga, J. M.; Schaller, R. D.; Werder, D.; Stewart, M. H.; Klimov, V. I.; Hollingsworth, J. A. *J. Am. Chem. Soc.* **2004**, *126*, 11752.
(56) Kovalenko, M. V.; Talapin, D. V.; Loi, M. A.; Cordella, F.; Hesser, G.; Bodnarchuk, M. I.; Heiss, W. *Angew. Chem., Int. Ed.* **2008**, *47*, 3029.